dynamical structural science

Photolysis of Br₂ in CCl₄ studied by time-resolved X-ray scattering

Qingyu Kong,[a] Jae Hyuk Lee,[b] Manuela Lo Russo,[c] Tae Kyu Kim,[d] Maciej Lorenc,[e] Marco Cammarata,[c] Savo Bratos,[f] Thomas Buslaps,[c] Veijo Honkimaki,[c] Hyotcherl Ihee[b] and Michael Wulff[c]*

[a]Synchrotron Soleil, Saint-Aubin, BP 48, 91192 Gif-sur-Yvette, France, [b]Center for Time-Resolved Diffraction, Department of Chemistry, Graduate School of Nanoscience and Technology (WCU), KAIST, Daejeon 305-701, Republic of Korea, [c]European Synchrotron Radiation Facility, BP 220, Grenoble 38043, France, [d]Department of Chemistry and Institute of Functional Materials, Pusan National University, Pusan, Republic of Korea, [e]Université de Rennes 1, Rennes 35042, France, and [f]Université Pierre and Marie Curie, 75252 Paris, France. Correspondence e-mail: wulff@esrf.fr

A time-resolved X-ray solution scattering study of bromine molecules in CCl₄ is presented as an example of how to track atomic motions in a simple chemical reaction. The structures of the photoproducts are tracked during the recombination process, geminate and non-geminate, from 100 ps to 10 µs after dissociation. The relaxation of hot Br₂* molecules heats the solvent. At early times, from 0.1 to 10 ns, an adiabatic temperature rise is observed, which leads to a pressure gradient that forces the sample to expand. The expansion starts after about 10 ns with the laser beam sizes used here. When thermal artefacts are removed by suitable scaling of the transient solvent response, the excited-state solute structures can be obtained with high fidelity. The analysis shows that 30% of Br₂* molecules recombine directly along the X potential, 60% are trapped in the A/A' state with a lifetime of 5.5 ns, and 10% recombine non-geminately *via* diffusive motion in about 25 ns. The Br—Br distance distribution in the A/A' state peaks at 3.0 Å.

1. Introduction

The high intensity of X-ray pulses from synchrotrons has opened up new opportunities for measuring molecular structure in physical, chemical and biological systems with 100 ps time resolution. Hard X-rays with wavelengths around 1 Å (12.4 keV) are mainly scattered (or diffracted) by localized electrons in atoms and the interference pattern from neighboring atoms is very sensitive to their relative position. The first multi-frame movie of a protein in action was realized in 1996 in a Laue diffraction study of the CO dynamics in myoglobin (Srajer *et al.*, 1996). This work was followed by a study in solution, the dissociation of I₂ in liquid CH₂Cl₂ (Neutze *et al.*, 2001). Time-resolved scattering has proven particularly successful and it has provided new insights in many interesting problems in chemistry and biology. Studies of ligand dynamics in hemoglobin (Cammarata *et al.*, 2008) and proton pumping in bacteriorhodopsin (Andersson *et al.*, 2009) have confirmed that scattering is a very useful complement to optical spectroscopy albeit at lower time resolution (100 ps *versus* 100 fs). Many small-molecule reactions have been studied recently and the reader is referred to Kim *et al.* (2009) for a review of X-ray scattering and to Chergui & Zewail (2009) for a review of ultra-fast X-ray science.

The ultimate dream is to visualize atoms in molecules that undergo a structural change. Atoms move inside molecules in femtoseconds, the timescale of molecular vibrations, which precludes their direct visualization with synchrotron radiation. In most cases synchrotrons can be used to measure the structure of longer-lived intermediates and their population dynamics. Finally synchrotrons are essential for preparing femtosecond experiments with free-electron lasers such as the LCLS at Stanford and the European XFEL in Hamburg.

Recent studies of the recombination dynamics of I₂ in CCl₄ have demonstrated the power and limitation of X-ray scattering in small molecules (Plech *et al.*, 2004; Wulff *et al.*, 2006). The recombination of I₂ was interpreted using atom–atom distribution functions $g_{ij}(r, t)$ which were calculated in parallel by molecular dynamics (MD) simulations. A strong duality between solute and solvent structures was found in reversible reactions: when the solute signals decrease as the molecules return to their initial state, the solvent signal increases owing to the rise in temperature from the heat release. Here we extend this study to Br₂ to determine its dissociation pathways in CCl₄ and to identify the problems associated with lower solute/solvent contrast. As the Br₂ molecule has $Z = 70$ electrons and CCl₄ has $Z = 74$, the (coherent) forward scattering,

$S(Q = 0)$, which is proportional to Z^2, is almost identical for the solute and the solvent molecule.

The photodissociation and recombination dynamics of diatomic molecules, especially molecular halogens, have long been considered a paradigm for a simple reaction dynamics involving breakage and formation of a bond (Kelley *et al.*, 1984; Abul-Haj & Kelley, 1986, 1987; Harris *et al.*, 1986; Lingle *et al.*, 1990). The simplicity of this reaction makes it an excellent choice for studying cage dynamics, the key element leading to efficient geminate recombination. While most of the studies in liquids have focused on molecular iodine owing to its larger extinction coefficient at visible wavelengths (about five times higher than in Br_2), there are only very few studies of bromine (Strong, 1965; Abul-Haj & Kelley, 1985; Zhu & Harris, 1991, 1993). Quantum chemical calculations have shown that Br_2 possesses a large number of electronic states (Mulliken, 1971; Bado *et al.*, 1984) as shown in Fig. 1. The states X, A, A' and B of Br_2 are attractive; the others, including the low-lying state $^1\pi_u$, are repulsive. The Br_2/CCl_4 solution was excited by a 150 fs pulse at 400 nm that promotes Br_2 into the B and $^1\pi_u$ states. The excited B state undergoes rapid (≤ 1 ps) solvent-induced predissociation along the $^1\pi_u$ repulsive potential energy surface (PES), producing a hot Br_2^* molecule with Br—Br distance around 4 Å. Two possible reactions take place at this stage: hot Br_2^* molecules are either trapped in the solvent cage where they relax to the ground state along the X potential through vibrational cooling while heating the solvent, or they relax into the A/A' state which is predicted to have an extended Br—Br distance of 2.65 Å. In both cases the Br atoms recombine geminately with their original partner. A smaller fraction of excited molecules escapes the cage and recombines with other partners in a diffusive process called non-geminate recombination. Laser spectroscopic studies by Strong (1965), Abul-Haj & Kelley (1985) and Zhu & Harris (1991, 1993) have shown that three timescales govern the recombination of bromine: 30% of the dissociated molecules recombine directly along the X potential with a time constant of $\tau_\alpha = 0.140$ ns; 60% are trapped in the A/A' state with a lifetime of $\tau_\beta = 5.5$ ns. Finally in 10% of cases, Br atoms escape the cage and recombine non-geminately. The reaction speed is concentration dependent and typically $\tau_\gamma = 5$ ns at 14 mM.

Chemical reactions in solution are different and richer than those in the gas phase owing to solvent interactions that might speed up or slow down certain reaction channels. It is important to investigate the influence of solute/solvent interactions by comparing the solute dynamics in different solvents, polar and non-polar, and compare the results with MD simulations. The structure of the solvent around a solute is probed by the so-called solute/solvent cross term. The signal cannot be measured alone without resonant scattering techniques, but it can be simulated by MD and expressed through atom–atom pair distribution functions $g_{ij}(r, t)$, where i is an atom in the solute and j is an atom in the coordination shell of the solvent (see Bratos *et al.*, 2004). In the present study, MD simulations were used to check the cage structure.

The recombination reaction of photodissociated halogens is readily studied by optical spectroscopy (Chuang *et al.*, 1974; Nesbitt & Hynes, 1982) which permits the detection of short-lived species with picosecond and sub-picosecond resolution. Unfortunately, visible light, with wavelengths in the hundreds of nanometres, interacts with outer-shell electrons making it impossible to determine the time-dependent structure without a model of the potential energy surface. By contrast, X-rays scatter from all the electrons in the sample, which means that all reaction pathways are probed in principle. That is not always the case in optical spectroscopy where selection rules might render certain reaction channels invisible. In X-ray scattering, in contrast, all intermediates are probed in proportion to their scattering cross sections and concentrations.

The organization of the paper is as follows: §2 discusses the experimental method and the MD simulations. §3 describes the data analysis. §4 presents the Br_2CCl_4 data; the discussion includes the recombination dynamics of Br atoms and the thermal expansion of the solvent. §5 compares the similarities and differences between Br_2 and I_2. A static measurement of the intramolecular and intermolecular structure of liquid CCl_4 with 88 keV X-ray diffraction is also presented. §6 gives a conclusion of the present work.
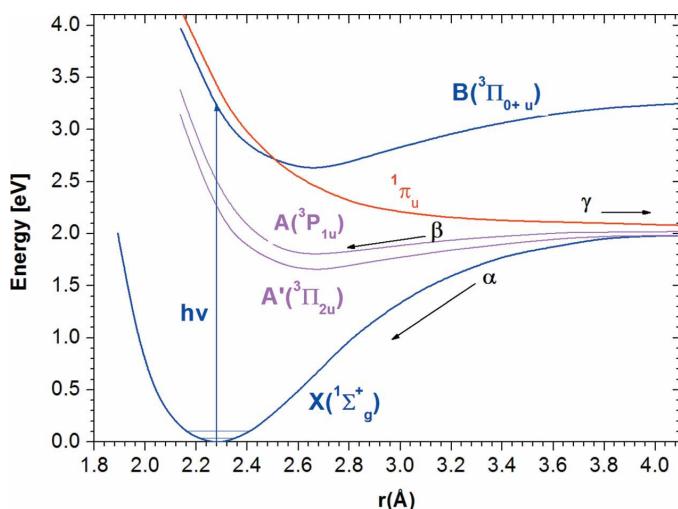

Figure 1
Low-lying electronic states for Br_2. Photoexcitation with blue light (400 nm) brings Br_2 to the excited states B and $^1\pi_u$ as shown by the blue arrow. The X, A/A' and B states are attractive and $^1\pi_u$ is repulsive. Three processes are involved in the recombination: α is the recombination in X *via* vibrational cooling in 0.14 ns, β passes though the A/A' states from where it decays in 5.5 ns into X. In γ, Br_2 dissociates into atoms that subsequently recombine non-geminately in 25 ns (10 mM concentration). Adapted from Mulliken (1971).

2. Experimental technique and MD simulations

2.1. Experimental technique

The experiments were performed with synchrotron radiation from beamline ID09B at the ESRF which has a pump–probe camera for scattering and diffraction that uses single pulses of X-rays (Schotte *et al.*, 2002; Wulff *et al.*, 2002, 2006).
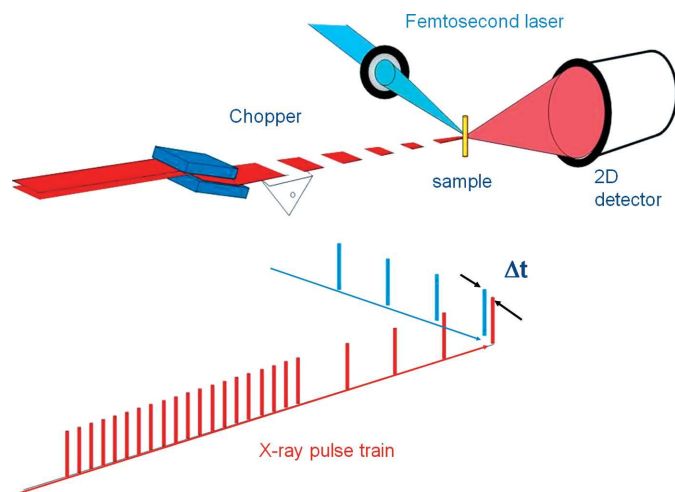
Figure 2

Principle of the picosecond camera on beamline ID09B at the ESRF. The Br_2CCl_4 solution is injected into the two beams through a capillary (or open jet). Ultra-short laser pulses are focused onto the sample to dissociate Br_2. The reaction is probed by delayed X-ray pulses from a monoharmonic undulator with a 3% bandwidth beam around 18.2 keV with 2×10^8 photons per pulse. The high-speed chopper selects X-ray pulses at 986.3 Hz and the scattered signal is recorded on an integrating CCD detector.

In a typical pump–probe experiment, a laser pulse initiates a physical or chemical process in the sample and a delayed X-ray pulse probes the structure at a given time delay. The X-ray signal is recorded on an integrating charge-couple device (CCD) detector without time resolution. In cyclic processes, the experiment is repeated at the cycling frequency which is typically 1–1000 Hz. In irreversible systems, the sample is scanned through the laser/X-ray beam which slows down the acquisition considerably owing to the time it takes to move the sample. This is the typical case for protein work where the capillary is scanned across the beam with a frequency of about 1 Hz. A schematic drawing of the pump–probe setup is shown in Fig. 2. Intense monochromatic ($\delta E/E = 0.014\%$) or pink ($\delta E/E = 3\%$) X-ray pulses are isolated from the pulse train from the synchrotron by a chopper (Cammarata *et al.*, 2009). The chopper can select single pulses (50–150 ps) from the timing-bunch modes at the ESRF or longer more intense super pulses (1–30 µs) (see Fig. 3). The laser pulses are produced in a Ti:sapphire femtosecond laser which is synchronized to the 352.2 MHz radio frequency (RF) of the storage ring. The oscillator produces 800 nm pulses at 88.05 MHz from which a sub-train at 986.3 Hz is amplified. The default frequency of the chopper and the laser is 986.3 Hz, the 360 sub-harmonic of the orbit frequency at the ESRF.

The Br_2CCl_4 experiments were carried out in 16-bunch mode with the pink beam from the U17 undulator. The undulator was operated at a 9 mm gap ($E_f = 18.2$ keV, $\delta E/E = 3\%$) to reduce the intensity of higher harmonics to below 1%. The undulator beam was focused by a platinum-coated toroidal mirror into a 100 µm (H) × 60 µm (V) spot with 2×10^8 photons per pulse. The incidence angle was 2.668 mrad and the reflected energy range was 0–26 keV. The spectra of
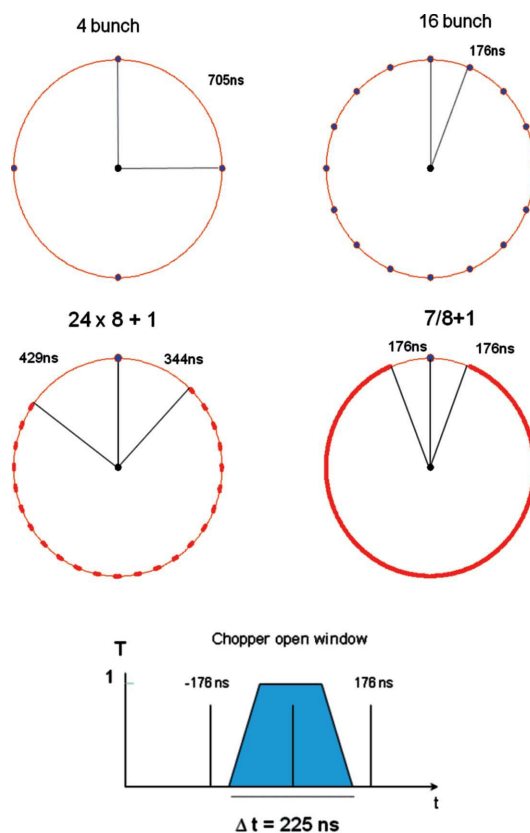

Figure 3

Synchrotron bunch structures used in pump–probe experiments with single X-ray pulses. The minimum time gap needed to isolate a single pulse is about 176 ns. In 2009, the four-bunch mode was used 6.3% of the time, 16-bunch 22.5%, hybrid 5.4% and 7/8+1 mode 48.6%. In the remaining 17.2%, the synchrotron was operated in uniform mode with 992 evenly spaced bunches. The chopper open window is shown at the bottom.

the U17 and U20 undulators at the minimum gap of 6 mm are shown in Fig. 4.

The focused beam was sent though the chopper, which is placed in the quasi-focused beam just in front of the sample. 400 nm and 150 fs laser pulses were used to dissociate Br_2 with a pulse energy of 130 µJ. The 400 nm beam was obtained by frequency doubling the 800 nm beam in a β-BaB_2O_4 (BBO) crystal.

A 0.3 mm-thick sheet of liquid Br_2CCl_4 was produced by a sapphire nozzle and the flow speed was adjusted to deliver a fresh sample for every new laser pulse. With a vertical focus of 0.06 mm, the minimum flow speed of 0.06 m s^{-1} was obtained with a pressure of 5 bar. The laser and X-ray pulses were synchronized as follows. The 225 ns open window of the chopper is first centered on a single pulse. The pulse separation in the 16-bunch mode is 176 ns so, with a rotation jitter as small as 3 ns (r.m.s.), pre- and post-pulses are completely removed. The beam is passed through a 165 mm-long tunnel in the chopper which is 0.14 mm high. The laser/X-ray delay was measured using a GaAs photodetector (Wrobel *et al.*, 1998) and recorded on a 6 GHz oscilloscope (see Fig. 5). The response of the detection chain to the ultra-short laser pulse is 150 ps (FWHM). The laser pulse is then moved onto the X-ray
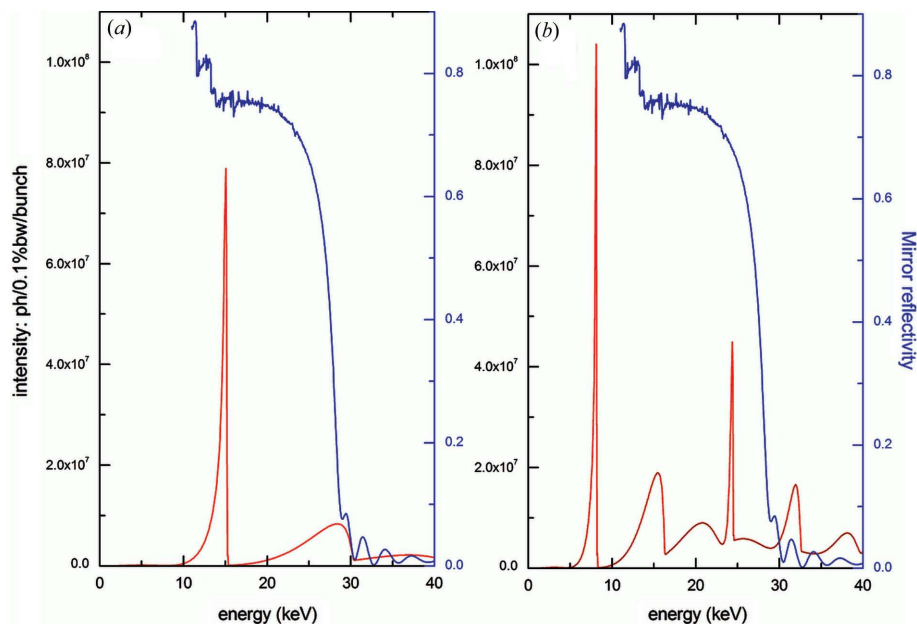
Figure 4
Spectral intensity from the in-vacuum undulators U17 (*a*) and U20 (*b*) at the ESRF. The intensity is calculated for one 5 mA bunch (14.1 nC). The reflectivity of the focusing mirror is shown in blue on the *y* scale on the right.
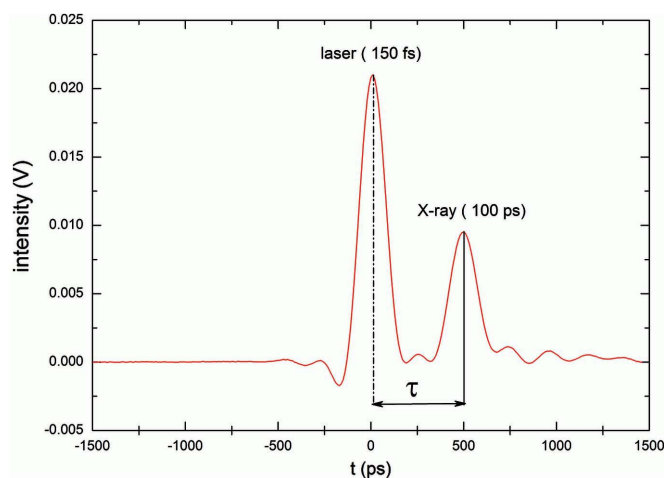

Figure 5
Measured delay between the laser and X-ray pulse. The pulses are detected with a GaAs photodetector and recorded on a 6 GHz oscilloscope (LeCroy Wavemaster 8620A). Note that the 150 fs laser pulse is broadened to 150 ps, which defines the resolution of the detection chain (detector, cable and oscilloscope).

temperature rise, as a function of the horizontal and vertical laser beam position. As the laser spot was larger than the 0.10×0.06 mm X-ray spot, only the central part of the laser-illuminated sample was probed by the X-ray beam, which improved the uniformity of the excitation. A 133 mm-diameter MarCCD detector was placed 43 mm from the sample and the 2θ scattering angle was measured from $1.5°$ to $57.1°$. With a center-of-mass wavelength in the pink spectrum of 0.698 Å, the q range is 0.23–8.61 Å^{-1} ($d_{min} = 0.73$ Å, $d_{max} = 27.3$ Å). The images were integrated azimuthally and corrected for polarization and space-angle effects. The exposure time was 6 s per frame. The exposure time was scaled to the decaying synchrotron current to have the same intensity on the CCD during the fill. The CCD images were collected in pairs with and without laser to minimize the effects of drift in the beamline and sample. As the induced signal from a small molecule is feeble, typically <1% of the solvent background, the data collection was repeated many times to improve the signal-to-noise ratio and to facilitate the statistical rejection of bad images.

2.2. MD simulation

The packing of CCl_4 around the reaction products $Br_2(X)$, $Br_2(A/A')$ and Br atoms was calculated by MD simulations using *MOLDY* (Refson, 2000). The Br—Br bond length in the X and A/A' states was 2.28 and 2.65 Å, respectively. The OPLS model for CCl_4 was used (Duffy *et al.*, 1992) in which CCl_4 is treated as a rigid tetrahedral molecule with a C—Cl bond length of 1.769 Å. The intermolecular interactions are described with atom-centered 6–12 Lennard–Jones potentials plus Coulomb potentials with partial charges on the C and Cl atoms. In the simulations, ground-state $Br_2(X)$, excited-state Br_2 (A/A') or two neutral Br atoms were surrounded by 512 CCl_4 molecules in a cubic box of linear size 43 Å. The simulations were performed at 300 K with a density of 1.595 g cm^{-3}. The scattered intensity of these candidate structures including their cages were calculated from the atom–atom distribution functions $g_{ij}(r)$ and the atomic form factors.

By coupling to a Nose–Hoover thermostat (Hoover, 1985), the systems were equilibrated for 20 ps at constant temperature. The simulations were performed in the NVT ensemble and the trajectories were followed up to 1 ns with a step size of 0.5 fs. Periodic boundary conditions were used and the van der Waals interaction was cut off above 11 Å.

The scattering curves from the heating of CCl_4 alone were measured separately with the same laser wavelength. The derivatives with respect to a temperature change at fixed

pulse by shifting the phase of the reference clock of the 88.05 MHz (RF/4) oscillator. The timing of the *Q* switch and the Pockels cells in the amplifier are also shifted to pick and amplify the correct pulse.

The concentration of the Br_2CCl_4 solution was as high as 0.138 *M* as required to obtain an optical density of 0.5 at 400 nm. At this concentration, 68% of the incoming laser beam is transmitted.

The laser was focused to 0.15×0.12 mm and the laser/X-ray spatial overlap was optimized by measuring the amplitude of $\Delta S(q, \tau)$ for $\tau = 1$ µs, which is proportional to the

pressure or a density change at fixed temperature were calculated in the same way as in our methanol study (Cammarata *et al.*, 2006).

3. Data analysis

3.1. Difference scattering signal $\Delta S(q, \tau)$

To extract the laser-induced signal, the difference scattering $\Delta S(q)$ was used to interpret the experimental data. $\Delta S(q, \tau)$ is the time-integrated X-ray energy flux S scattered in a given solid angle in the presence of the laser pump pulse minus the time-integrated X-ray energy flux S_0 in the absence of the pump. It depends on two variables, the modulus of the scattering wavevector, $q = 4\pi \sin\theta / \lambda$, where 2θ is the scattering angle and λ is the X-ray wavelength, and τ, which is the time delay between the laser and the X-ray pulse. The measured scattering curves and their Fourier transforms are shown in Fig. 6.

The time-resolved diffraction theory by Bratos was employed to describe the experimental data (Bratos *et al.*, 2002, 2004). In the quasi-static limit, in which the 150 fs laser is assumed to be much faster than the chemical reaction, the difference signal $\Delta S(q, \tau)$ is

$$\Delta S(q, \tau) = \int\limits_{-\infty}^{+\infty} I_X(t - \tau)\Delta S_{inst}(q, t)\,dt,$$

$$\Delta S_{inst}(q, t) = \left(\frac{e^2}{mc^2}\right)^2 p \left(\sum_{\mu \neq \nu} f_\mu f_\nu \left\{ \frac{1}{V(t)} \int_0^\infty dr\, 4\pi r^2 \right. \right.$$
$$\times \left[g_{\mu\nu}(r, t) - 1 \right] \frac{\sin qr}{qr}$$
$$\left. \left. - \frac{1}{V(0)} \int_0^\infty dr\, 4\pi r^2 \left[g_{\mu\nu}^0(r) - 1 \right] \frac{\sin qr}{qr} \right\} \right), \quad (1)$$

where $I_X(t - \tau)$ is the temporal X-ray profile for a laser/X-ray delay of τ, $\sum$ denotes the summation over interatomic distances $r_{\mu\nu} = r_\mu - r_\nu$ between pairs of atoms, and $f_\mu = f_\mu(q)$ denotes the atomic form factor of the atom μ.

To extract the change in the radial electron density, the sine-Fourier transform $\Delta S(r, \tau)$ is calculated from the measured $\Delta S(q, \tau)$ as

$$\Delta S(r, \tau) = \frac{1}{2\pi^2 r} \int_0^\infty dq \left[\sum_{\mu \neq \nu} f_\mu(q) f_\nu(q) \right]^{-1} q\Delta S(q, \tau)\sin(qr),$$
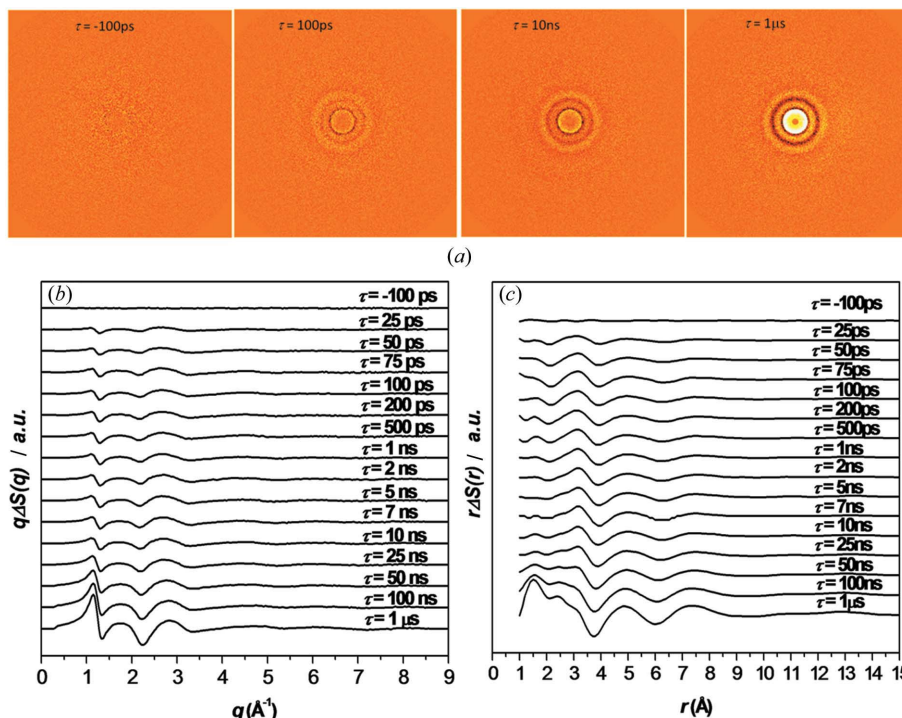$$(2)$$

Figure 6
Time-resolved scattering signals for Br$_2$ in CCl$_4$. (*a*) Raw difference images for $\tau = -100$ ps, 100 ps, 10 ns and 1 μs. The change in density from the onset of thermal expansion is clearly seen in the 1 μs image as the white disc around the beamstop in the center. (*b*) Difference intensity, $q\Delta S(q, \tau)$ after image normalization at high Q. (*c*) Radial density, $r\Delta S(r, \tau)$ from the sine-Fourier transform of $q\Delta S(q, \tau)$.

where $\left[\sum_{\mu \neq \nu} f_\mu(q) f_\nu(q) \right]^{-1}$ is the sharpening function which serves to normalize out the damping effect of the atomic form factors. In that form, $\Delta S(r, \tau)$ is almost identical to the statistical atom–atom functions $g_{ij}(r, t)$ used in MD simulations. By sine-Fourier transforming equation (1) we obtain

$$\Delta_{inst} S(r, t) = \left(\frac{e^2}{mc^2}\right)^2 p \left\{ \sum_{\mu \neq \nu} w_{\mu\nu} \times \left[\frac{1}{V(t)} g_{\mu\nu}(r, t) \right. \right.$$
$$\left. - \frac{1}{V(0)} g_{\mu\nu}^0(r) \right] - \left[\frac{1}{V(t)} - \frac{1}{V(0)} \right] \right\},$$

$$w_{\mu\nu} = f_\mu f_\nu \left(\sum f_\mu f_\nu \right)^{-1}, \quad (3)$$

where $w_{\mu\nu}$ are weight coefficients and $V(t)$ is the volume of the system at time t. The first term gives the change in the pair distribution functions during the chemical reaction, the second gives the change in the volume owing to laser heating. During a chemical reaction, the $g_{\mu\nu}$ for μ and ν atoms that are side-by-side in the molecules will stand out in the difference map. Owing to the induced expansion of the sample, the second term cannot be neglected. Equation (3) is central to time-resolved X-ray scattering. It shows how the time dependence of $g_{\mu\nu}(r, \tau)$ is related to the Fourier transform of the scattered intensity.

The scattered signal is modeled as a sum of two terms, $\Delta S(q, \tau) = \Delta S(q, \tau)_{Bromine} + \Delta S(q, \tau)_S$. The first term describes Br$_2$ in its cage and the other is the time-dependent
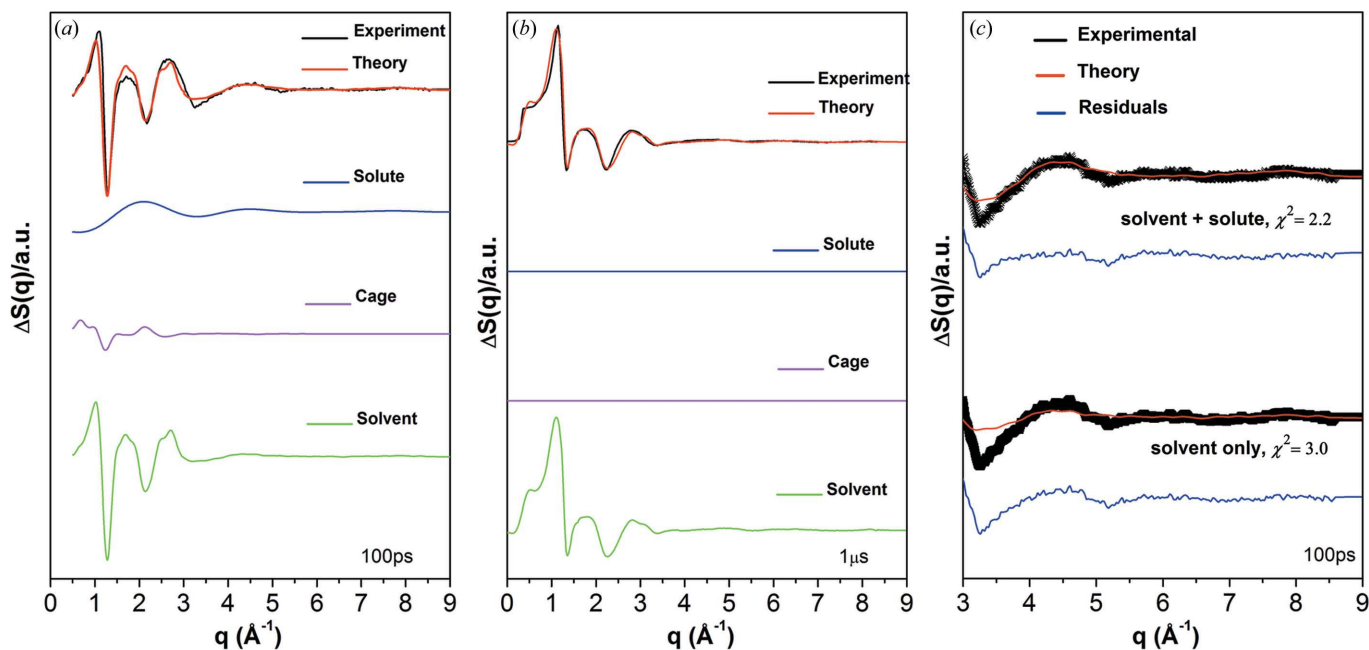
Figure 7
(*a*) Contributions to the signal 100 ps after dissociation. (*b*) Contributions to the signal 1 μs after dissociation. The black curves are measured, blue and purple are MD simulated. The green curves are thermal solvent differentials from separate experiments on the pure solvent. The red curves are the sum of the blue, purple and green. (*c*) Residuals between theory and experiments are shown with and without solute. Inclusion of the weak solute signal improves χ^2 significantly.

response from the solvent. The $\Delta S(q, \tau)_{\text{Bromine}}$ term was simulated by MD as described in §2. The temperature rise before 10 ns and the thermal expansion after 10 ns were determined by fitting the experimental solvent derivatives $[\partial S(q)/\partial T]_\rho$ and $[\partial S(q)/\partial \rho]_T$ to the experimental data as described in our previous study (Cammarata *et al.*, 2006; Landau & Lifshitz, 1959). The solute and solvent terms in q space are shown in Fig. 7 for 100 ps and 1 μs. The $\Delta S(q, \tau)$ and $\Delta S(r, \tau)$ curves are shown in Figs. 8(*a*) and Fig. 8(*b*), respectively, for time delays of 100 ps, 1 ns and 1 μs together with the populations dynamics in Fig. 8(*c*). The hydrodynamics of the solvent, *i.e.* the $\Delta T(\tau)$ and $\Delta \rho(\tau)$ curves, are shown in Fig. 9.

4. Results and discussion

To follow the structural evolution of bromine, time-resolved data were collected for 17 time delays: −3 ns, −100 ps, 25 ps, 50 ps, 75 ps, 100 ps, 200 ps, 500 ps, 1 ns, 2 ns, 5 ns, 7 ns, 10 ns, 25 ns, 50 ns, 100 ns and 1 μs. The −3 ns delay, where the X-rays arrive before the laser, served to check the noise floor in the experiment. A second negative time delay, −100 ps, was collected to check the stability of time zero. As the laser and X-ray beams were quasi-parallel, the early time points 0 ps, 25 ps, 50 ps and 75 ps are special in that the 150 fs laser pulse 'cleaves' the 100 ps-long X-ray pulse in two parts: the front records the non-excited sample and the back records the excited sample with a truncated X-ray profile. That method hinges on having a very short laser pulse and a very low jitter between the laser and X-ray pulse. It can be used to probe intermediates with lifetimes slightly below the X-ray pulse length of 100 ps.

The difference signals were generated by subtracting the reference data at −3 ns from the data at each time delay. Fig. 6(*b*) shows the difference signals $q\Delta S(q, t)$, the quantity that enters in the Fourier transform. The image at −100 ps shows no difference intensity. At positive times, difference features emerge and progress with time. The Fourier transform, shown here as $r\Delta S(r, \tau)$, probes the change in the radial distribution of the atomic pairs Br—Br, Cl—Cl and Br—Cl from the laser excitation. The weak negative peak at 2.17 Å is from the depletion of parent Br$_2$(X). It is seen more clearly in the theoretical fits for the 100 ps and 1 ns curves in Fig. 8(*b*). The positive peak at 3.00 Å contains contributions from the A/A' states in their cages and from the solvent bulk, *i.e.* from the increase in temperature.

To obtain the evolution of bromine in the α, β and γ processes shown in Fig. 1, the experimental data were fitted to a theoretical model: the total change in the scattering was assumed to be the sum of the following structure differentials,

$$\Delta S(q, \tau) = \Delta S(q, \tau)_{\text{Bromine}} + \Delta S(q, \tau)_{\text{S}}, \qquad (4)$$

where

$$\Delta S(q, \tau)_{\text{Bromine}} = n_\alpha \, \Delta S_\alpha(q, \tau) + n_\beta(\tau) \, \Delta S_{\text{Br2},\beta}(q) + n_\gamma(\tau) \, \Delta S_\gamma(q) \qquad (5)$$

and

$$\Delta S(q, \tau)_{\text{S}} = [\partial S(q)/\partial T]_\rho \, \Delta T(\tau) + [\partial S(q)/\partial \rho]_T \, \Delta \rho(\tau). \qquad (6)$$

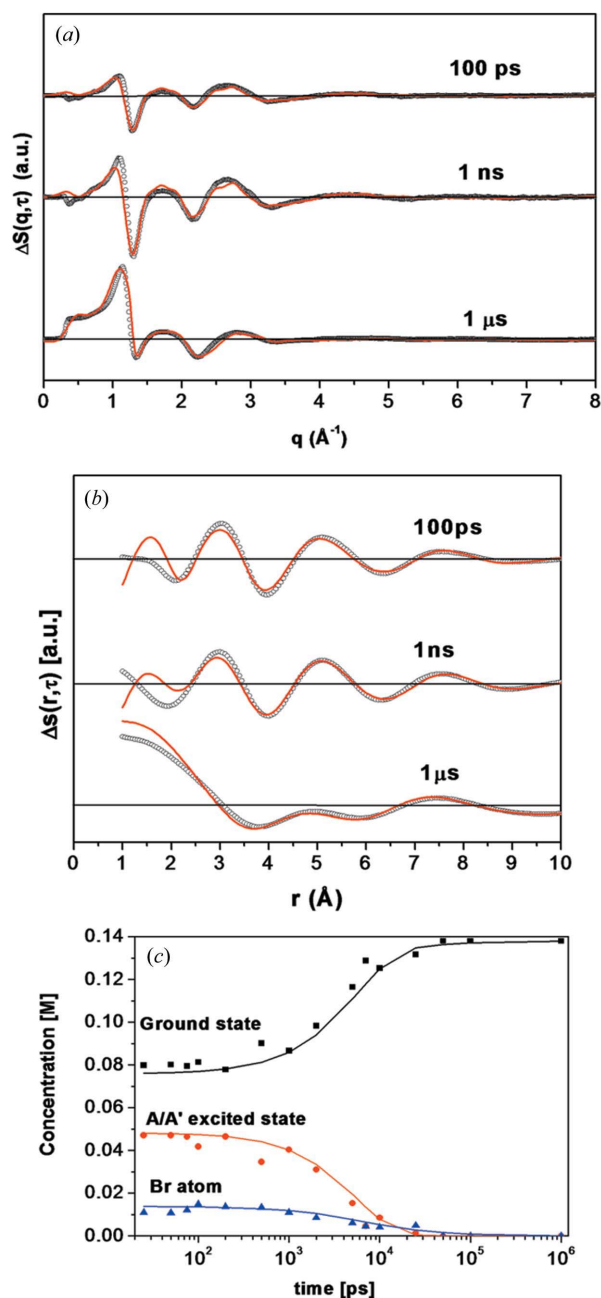Equation (5) assumes that β and γ decay to the ground state in times much shorter than their excited-state lifetime (popula-
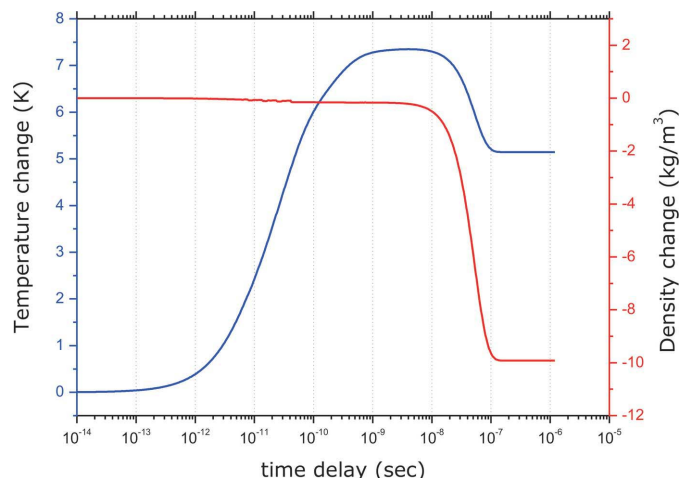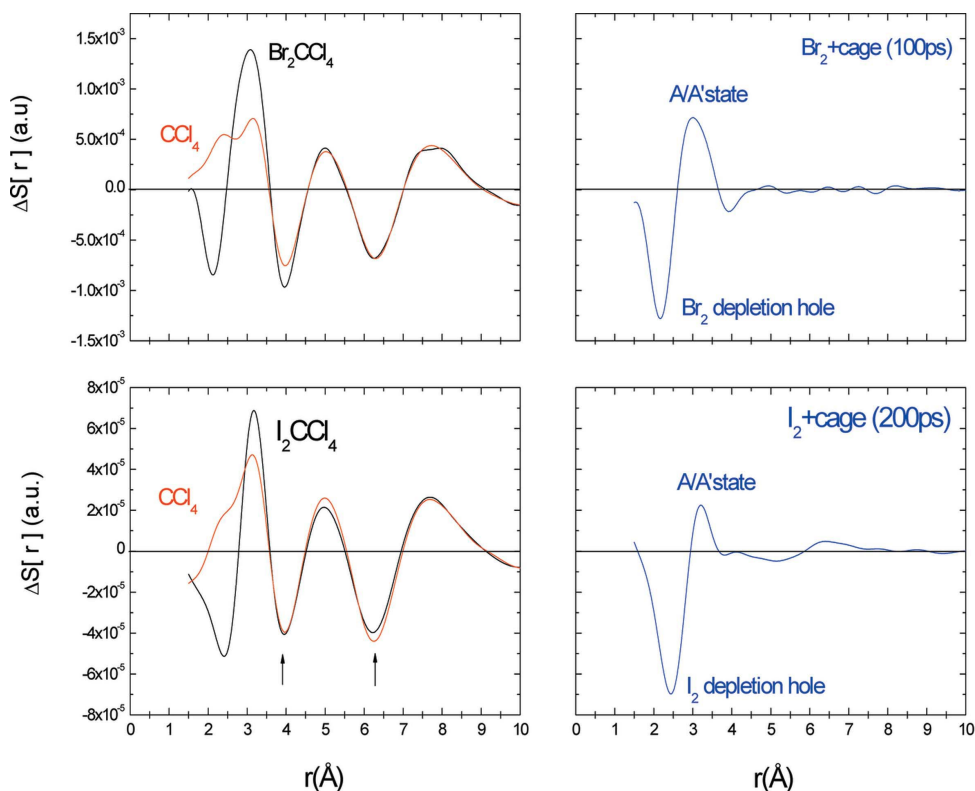
Figure 9
Hydrodynamic changes in the Br_2CCl_4 solution. The calculated temperature and density curves have been fitted to the experimental $\Delta S(q, \tau)$ curves. Note how the temperature increases from 10–500 ps from the vibrational cooling of Br_2^* in the X state. The sample begins to dilute (expand) after 10 ns. The temperature starts to drop, caused by the expansion, after about 50 ns.

Figure 8
(a) $\Delta S(q, \tau)$ at 100 ps, 1 ns and 1 µs. After 1 µs, all molecules and atoms have recombined into Br_2. The remnant signal is thermal and ascribed to a reduction in solvent density. (b) The change in the atom–atom pair distribution $\Delta S(r, \tau)$ for τ = 100 ps, 1 ns and 1 µs before the solvent is removed. The black curves show the experimental data, red curves are theoretical. (c) The concentration of the ground state X, excited state A/A' and of Br atoms as a function of time. The populations were determined from the scattering with MD calculated transitions using least-squares refinement. The solid curves are calculated from a kinetic model.

tion dynamics). By varying n_α, n_β and n_γ and applying least-square refinement, the deduced population changes in the α, β and γ states are shown in Fig. 8(c). The analysis shows that 30% of excited bromine molecules recombine along the X potential through vibrational cooling, 60% are trapped in the A/A' states and recombine geminately, and 10% escape the

cage and recombine non-geminately, indicating that the potential barrier of the CCl_4 cage traps bromine atoms very efficiently. The lifetime of the A/A' state is 5.5 ns and the Br atoms recombine non-geminately with a 5 ns time constant at this (initial) concentration of 0.014 M. The time constant for the vibrational cooling needs further analysis but it seems consistent with the laser spectroscopy value of 140 ps. These figures agree with laser spectroscopic data.

The theoretical fits are shown in Figs. 8(a) and 8(b); the fits are fair but not perfect. The fits have improved substantially compared with the I_2CCl_4 study where the thermal solvent response was simulated by MD. In this study, the thermal solvent differentials were measured by exciting overtones of the C—Cl stretch band in CCl_4 with ultra-short laser pulses at 400 nm. Heat is injected into the molecules without any structural change on the times studied here above 100 ps. In Fig. 10 we show how the pure solute signal for Br_2^* can be recovered, with high fidelity, by scaling the $\Delta S(r, \tau)$ curves for Br_2CCl_4 and pure CCl_4 to each other at high r values, i.e. at distances greater than the size of Br_2. At distances above 7 Å, the structural change in the two systems must be identical. For $r > 7$ Å, the Br_2CCl_4 signal $\Delta S(r, 100 \text{ ps})$ is purely thermal. Note how the Br_2^* + cage curve on the right in Fig. 10 shows ground-state depletion with a negative peak at 2.17 Å and how the A/A' state appears at 3.00 Å after 100 ps. The equivalent curves are shown for iodine below. The I_2 depletion is found at 2.44 Å and the less populated A/A' state is found at 3.20 Å.

We finally note that the (early time) solvent differential at constant volume has a simple geometrical interpretation in CCl_4. Note the two negative peaks indicated by arrows in the CCl_4 curve in Fig. 10. These minima coincide with the two intermolecular peaks in the radial map of liquid CCl_4 shown in Fig. 11. This (static) map has peaks at 3.8 and 6.1 Å that we attribute to distribution of Cl···Cl distances in the first coordination shell. The existence of these peaks shows that CCl_4 is

Figure 10
Recovering the solute signal by subtracting the solvent from the total signal. In the upper plot on the left, the measured radial change for Br_2CCl_4 is shown in black ($\tau = 100$ ps). The CCl_4 part, shown in red, is scaled to the black in the high-r limit. The solute + cage structure is shown on the right. It is the change in the radial electron density seen by an average excited atom in the solution. Note that the position of the bromine hole is smaller than in iodine and that the A/A' state occupancy is two to three times higher for bromine.
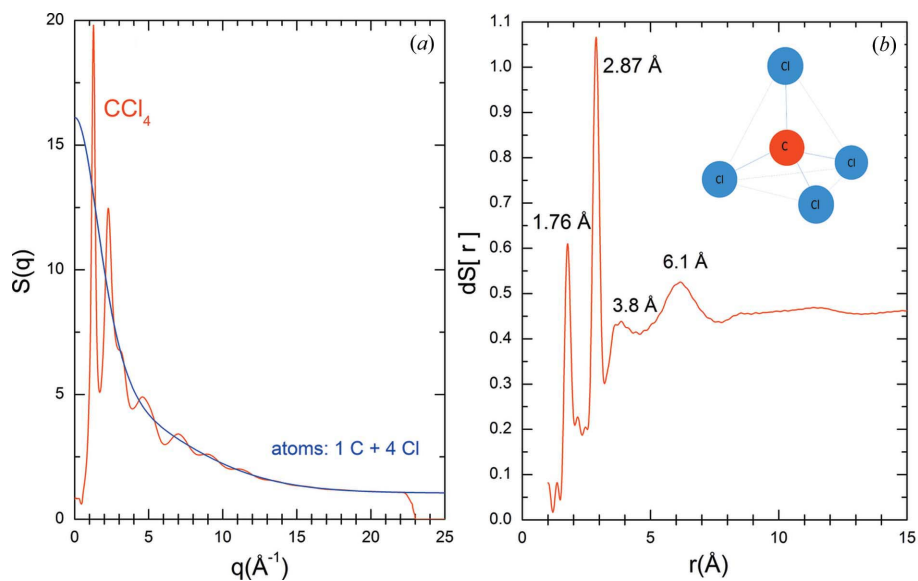
Figure 11
High-resolution scattering from CCl_4 measured at 88 keV (0.14 Å). This static measurement was performed on ID15 at the ESRF. The X-rays were recorded on a MAR imaging plate. (*a*) The liquid scattering is shown in red. The incoherent atomic gas scattering is shown in blue. (*b*) The sine-Fourier transform of the difference between the red and blue curves in (*a*) is a radial map of CCl_4 taken with X-rays (Kong *et al.*, 2005). The map shows both intramolecular and intermolecular atom–atom distances in CCl_4. The peak at 1.76 Å is the C—Cl bond, the 2.87 Å peak is the Cl—Cl correlation inside CCl_4. The broad peaks at 3.8 and 6.1 Å are assigned to the distance distribution of Cl···Cl pairs in the first coordination shell. The transient thermal response, at constant volume, is largely due to the broadening of these two Cl···Cl correlations which explains the two negative solvent peaks in $dS(r, \tau)$ at 3.8 and 6.1 Å in Fig. 10.

a highly ordered liquid. When the solvent temperature rises at constant volume at early times < 10 ns, the Cl···Cl distribution broadens constrained to constant volume (no time for expansion yet). That explains why the time-resolved solution data have negative peaks around 3.8 and 6.1 Å. With a suitable calibration, the amplitude of the solvent peaks can be used to determine the (average) temperature of the solvent.

5. Similarities and differences between Br_2 and I_2

The branching ratios for the α, β and γ processes for bromine in CCl_4 were determined to be 30, 60 and 10% when the dissociation is performed at 400 nm. The equivalent figures for iodine are 70, 20 and 10% (Plech *et al.*, 2004) at 530 nm. The difference can be understood from the potential energy curves for Br_2 and I_2 (Abul-Haj & Kelley, 1985). Predissociation of the iodine B state results in atoms with a kinetic

energy of 3600 cm^{-1}, while in bromine the recoil energy is 400 cm^{-1}. The energy drop in the repulsive curves of Br$_2$ is thus smaller than in I$_2$. The bromine atoms have shorter internuclear distances, which increases the probability of curve crossing from the repulsive states to the low lying A/A' states. Furthermore, smaller internuclear distances and lower recoil energies lower the possibility of cage escape of bromine atoms. The 5.5 ns lifetime of the A/A' state for bromine is longer than that for iodine with 2.7 ns. The longer lifetime of bromine is attributed to the deeper A/A' well than in iodine (Abul-Haj & Kelley, 1985).

6. Conclusion

The recombination of dissociated bromine molecules in CCl$_4$ was followed with 100 ps X-ray pulses from a synchrotron. 60% of excited Br$_2$ molecules are trapped in the A/A' state, while 10% escape the solvation cage to form neutral Br atoms. Compared with iodine, the longer lifetime and higher population of bromine trapped in the A/A' state comes from the deeper well depth and the lower recoil energy of bromine. The thermal expansion and temperature change of the solvent, owing to the energy released from the recombining molecules, were detected in real time. The oscillations at 3.8 and 6.1 Å in the high-r region come from intermolecular Cl$\cdots$Cl structural rearrangements in liquid CCl$_4$ during the adiabatic heating of the solvent under constant volume. The intermolecular structure of CCl$_4$ measured with 88 keV X-ray scattering confirms this conclusion. The temperature rise in CCl$_4$ is 6.3 K as compared with 3.0 K observed in iodine.

References

Abul-Haj, N. A. & Kelley, D. F. (1985). *Chem. Phys. Lett.* **119**, 182–188.
Abul-Haj, N. A. & Kelley, D. F. (1986). *J. Chem. Phys.* **84**, 1335–1344.
Abul-Haj, N. A. & Kelley, D. F. (1987). *J. Phys. Chem.* **91**, 5903–5905.
Andersson, M., Malmerberg, E., Westenhoff, S., Katona, G., Cammarata, M., Wöhri, A., Ewald, F., Eklund, M., Wulff, M., Davidsson, J. & Neutze, R. (2009). *Structure*, **17**, 1265–1275.
Bado, P., Dupuy, C., Magde, D., Wilson, K. R. & Malley, M. M. (1984). *J. Chem. Phys.* **80**, 5531–5538.
Bratos, S., Mirloup, F., Vuilleumier, R. & Wulff, M. (2002). *J. Chem. Phys.* **116**, 10615–10625.
Bratos, S., Mirloup, F., Vuilleumier, R., Wulff, M. & Plech, A. (2004). *Chem. Phys.* **304**, 245–251.
Cammarata, M., Ewald, F., Eybert, L., Reichenbach, W., Wulff, M., Anfinrud, P. A., Schotte, F., Kong, Q., Lindenau, B., Rabiger, J. & Polachowski, S. (2009). *Rev. Sci. Instrum.* **80**, 015101.
Cammarata, M., Levantino, M., Schotte, F., Anfinrud, P. A., Ewald, F., Choi, J., Cupane, A., Wulff, M. & Ihee, H. (2008). *Nat. Methods*, **5**, 881–886.
Cammarata, M., Lorenc, M., Kim, T. K., Lee, J. H., Kong, Q., Pontecorvo, E., Lo Russo, E., Schiró, G., Cupane, A., Wulff, M. & Ihee, H. (2006). *J. Chem. Phys.* **124**, 124504.
Chergui, M. & Zewail, A. (2009). *Chem. Phys. Chem.* **10**, 28–43.
Chuang, T. J., Hoffman, G. W. & Eisenthal, K. B. (1974). *Chem. Phys. Lett.* **25**, 201–205.
Duffy, E. M., Severance, D. L. & Jorgensen, W. L. (1992). *J. Am. Chem. Soc.* **114**, 7535–7542.
Harris, A. L., Berg, M. & Harris, C. B. (1986). *J. Chem. Phys.* **84**, 788–806.
Hoover, W. (1985). *Phys. Rev. A*, **31**, 1695–1697.
Kelley, D. F., Abul-Haj, N. A. & Jang, D. J. (1984). *J. Chem. Phys.* **80**, 4105–4111.
Kim, T. K., Lee, J. H., Wulff, M., Kong, Q. & Ihee, H. (2009). *Chem. Phys. Chem.* **18**, 1958–1980.
Kong, Q. Y., Kim, J., Lorenc, M., Kim, T. K., Ihee, H. & Wulff, M. (2005). *J. Phys. Chem. A*, **109**, 10451–10458.
Landau, L. D. & Lifshitz, E. M. (1959). *Course of Theoretical Physics: Fluid Mechanics.* Oxford: Pergamon Press.
Lingle, R. L. Jr, Xu, X., Yu, H., Zhu, X. R. & Hopkins, J. B. (1990). *J. Chem. Phys.* **93**, 5667–5680.
Mulliken, R. (1971). *J. Chem. Phys.* **55**, 288–309.
Nesbitt, D. J. & Hynes, J. T. (1982). *J. Chem. Phys.* **77**, 2130–2143.
Neutze, R., Wouts, R., Techert, S., Davidson, J., Kocsis, M., Kirrander, A., Schotte, F. & Wulff, M. (2001). *Phys. Rev. Lett.* **87**, 195508.
Plech, A., Wulff, M., Bratos, S., Mirloup, F., Vuilleumier, R., Schotte, F. & Anfinrud, P. A. (2004). *Phys. Rev. Lett.* **92**, 125505.
Refson, K. (2000). *Comput. Phys. Commun.* **126**, 309–329.
Schotte, F., Techert, S., Anfinrud, P. A., Srajer, V., Moffat, K. & Wulff, M. (2002). *Third-Generation Hard X-ray Synchrotron Radiation Sources*, edited by D. Mills, p. 345. New York: Wiley.
Srajer, V., Teng, T., Ursby, T., Pradervand, C., Ren, Z., Adachi, S., Schildkamp, W., Bourgeois, D., Wulff, M. & Moffat, K. (1996). *Science*, **274**, 1726–1729.
Strong, R. L. (1965). *J. Am. Chem. Soc.* **87**, 3563–3567.
Wrobel, R., Brullot, B., Dainciart, F., Doublier, J., Eloy, J.-F., Marmoret, R., Villette, B., Mathon, O., Tucoulou, R. & Freund, A. K. (1998). *Proc. SPIE*, **3451**, 156–161.
Wulff, M., Bratos, S., Plech, A., Vuilleumier, R., Mirloup, F., Lorenc, M., Kong, Q. & Ihee, H. (2006). *J. Chem. Phys.* **124**, 034501.
Wulff, M., Plech, A., Eybert, L., Randler, R., Schotte, F. & Anfinrud, P. (2002). *Faraday Discuss.* **122**, 13–26.
Zhu, X. R. & Harris, J. M. (1991). *Chem. Phys. Lett.* **186**, 183–188.
Zhu, X. R. & Harris, J. M. (1993). *J. Phys. Chem.* **97**, 6650–6655.